ADVANCED MATERIALS

Supporting Information

for *Adv. Mater.*, DOI: 10.1002/adma.201704629

High-Strength Nanotwinned Al Alloys with 9R Phase

*Qiang Li, Sichuang Xue, Jian Wang, Shuai Shao, Anthony H. Kwong, Adenike Giwa, Zhe Fan, Yue Liu, Zhimin Qi, Jie Ding, Han Wang, Julia R. Greer, Haiyan Wang, and Xinghang Zhang**

Supporting Information

High-strength nanotwinned Al alloys with 9R phase

*Qiang Li, Sichuang Xue, Jian Wang, Shuai Shao, Anthony H. Kwong, Adenike Giwa, Zhe Fan, Yue Liu, Zhimin Qi, Jie Ding, Han Wang, Julia R. Greer, Haiyan Wang and Xinghang Zhang**

Supporting Information
Supporting Information is available from the Wiley Online Library or from the author.

Figure S1. Microstructural and crystallographic information of Al-xFe (x = 1-10 at.%) films.
Figure S2. XRD pole figure measurements of the Al-xFe (x = 1-10 at.%) films.
Figure S3. Microstructure of Al-5.9 at.% Fe.
Figure S4. The Hall-Petch plot for the Al-Fe specimens and the selected ufg and nc monolithic Al and Al-xFe alloys processed *via* different techniques and hardness *vs.* solute atom concentration of various sputtered Al alloys with selective solutes.
Figure S5. Methodology to estimate the true stress-strain curves of the deformation volume of nt Al-xFe alloys.
Figure S6. *Ex situ* pillar compression results of monolithic Al and Al-xFe (x = 2.5 and 5.9 at.%) specimens.
Figure S7. Demonstration of fabrication of 20 μm thick Al-6 at.% Fe coating on Si wafer and *in situ* compressions on 3 μm micropillars of Al-6 at.% Fe specimens.
Figure S8. Atomistic structures for calculations of bulk stacking fault energies (SFEs), SFEs of Al as a function of in-plane atomic percentage of Fe, atomistic configurations to calculate the SFEs of surface atomic clusters, schematic representation of the paths of the surface trimer and septmer for the calculation of their SFEs and excess energy per surface atom *vs.* reaction coordinate curves for various types of surface atomic clusters for Al-3.1at% Fe.
Figure S9. MD simulations: 9R stability in monolithic nt Al and Al-5%Fe at room temperature and calculated compressive stress *vs.* strain curves of pure Al and Al-5%Fe.
Figure S10. Super X EDS and STEM of the Al-2.5%Fe (cross-sectional STEM) and post-mortem TEM micrographs of deformed Al-2.5 at.% Fe.
Table S1. Summary of columnar grain size, hardness and modulus of the pure Al and Al-Fe alloys. Compositions are all in atomic percentage.
Table S2. Details of atomistic models shown in Figure S8.
Movie S1. In situ compression of pure Al.
Movie S2. In situ compression of Al-2.5at.% Fe.
Movie S3. In situ compression of Al-5.9at.% Fe.

Movie S4. 3D MD simulation of 9R recovery in pure nt Al at ambient condition.
Movie S5. 3D MD simulation of 9R stability in nt Al-5 at.% Fe at ambient condition.
Movie S6. 3D MD simulation of uniaxial compression of nt Al-5 at.% Fe.
Movie S7. 2D MD simulation of uniaxial compression of Al-5 at.% Fe.

Density function theory (DFT) calculations

Validation of Pseudo potentials

Density function theory calculations were carried out using open source Quantum-ESPRESSO code.[1] Generalized gradient approximation (GGA) for exchange correlation functional with Perdew-Becke-Erzenhof (PBE) parameterization were employed in the calculations.[2] Interaction between valence electrons and ionic cores is treated with projector augmented wave (PAW) method. The pseudopotential files are obtained from the standard solid state pseudopotentials (SSSP) project, which selects and recommends pseudopotentials with reasonably good efficiency and accuracy towards basic physical properties including formation energy of solid and equation of state.[3] The numbers of valence electrons in the pseudo potentials for Al and Fe are 3 ($3s^2$, $3p^1$) and 16 ($3s^2$, $4s^2$, $3p^6$, $3d^6$), respectively. We use a plane wave energy cutoff of 408 and 1225 eV for Al and Fe, respectively, for calculations of lattice constants as well as the cohesive energies.

Such properties, calculated using the pseudopotentials are reported and compared to experimental values in **Table S**2. At ground state, Al has an FCC structure, while Fe has BCC structure. The lattice parameter and the cohesive energy of FCC Al was found to be 4.040 Å and 3.23 eV, in good agreement with experimentally measured values of 4.046 Å and 3.39 eV.[4] The properties of BCC Fe were found to be 2.816 Å and 4.71 eV, which agree reasonably well with

experimental values of 2.855 Å and 4.28 eV.[5] In addition, the results from our calculations fall well within the range of other DFT calculations.

Bulk stacking fault energies (SFEs)

We have examined the bulk SFEs on (111) planes of pure Al, as well as Al with different compositions of Fe impurity. For all cases, a total of 8 (111) atomic monolayers in y direction are considered. Periodic boundary conditions are applied in all directions. A vacuum of 8 Å is created between the top and bottom free surfaces of the crystal. To measure the SFE, the pristine structure is first relaxed to obtain the reference energy. The structure is then sheared at the 4^{th} and 5^{th} (111) plane to create a SF and subsequently relaxed. The bulk SFE is calculated based on the energy difference between the structures. For the case of pure Al (**Figure S**8a), a total of 32 atoms (4 per layer) are modeled. To model the Fe impurity (**Figure S**8a), an Al atom on one side of the slip plane is replaced by an Fe atom. The models in **Figure S**8a are of different size, hence different atomic percentage of Fe on a single (111) monoatomic plane.

The details of the models are summarized in **Table S**2.

The calculated stacking fault energy *vs.* in-plane atomic percentage of Fe is plotted in Figure S8b. For pure Al, the stacking fault energy is 128 mJ/m^2, in good agreement with the experimental values of 120-144 mJ/m^2.[4] This validation proves that 8 monoatomic layers are sufficient to reproduce the bulk stacking fault energy. The stacking fault energy increases with increasing Fe content. When Fe is at the in-plane atomic percentage of 25%, the stacking fault energy is as high as 178 mJ/m^2. Also, the increase in stacking fault energy is non-linear, the rate of increase also increases with higher Fe content. It is suspected that the interaction between neighboring Fe atoms may play an important role in the rapid increase in stacking fault energy.

Indeed, when the in-plane atomic percentage of Fe is 25%, the Fe atoms are merely separated by one layer of Al atoms.

Generalized stacking fault energies (SFEs) of surface atomic clusters

The SFEs of surface atomic clusters are calculated using surface trimer and septmer (pure and impure Al in **Figure S**8c) configurations. For all surface cluster models, two atomic monolayers of {111} Al are used as substrate in the x-z plane. For trimer models, each monolayer contains 16 atoms. For septmer models, each monolayer contains 36 atoms. The bottom monoatomic layer is fixed. The stable SFEs are first obtained for each model by calculating total energies of the models corresponding to perfect FCC and faulted stacking (**Figure S**8b). Total surface relaxation is allowed during the energy minimization. The obtained equilibrium (FCC stacking) and metastable structures, *i.e.* SFs, are then linearly interpolated to produce a chain of transient states. Each transient state is relaxed while fixing the motion of all the "mobile" atoms in the x-z plane and allowing them to move in the y direction.

The obtained excess energy per surface atom curves are shown in **Figure S**8e. The horizontal axis is the reaction coordinate, which corresponds to the position of the surface atomic cluster from its perfect FCC stacking. Therefore, at Coordinate 6, the cluster is at its metastable stacking fault configuration. It is evident from **Figure S**8 (comparing the black and blue curves) that the Trimers have to overcome higher energy barriers (by 0.012 eV on average) when they migrate from the perfect FCC configuration to a stacking fault configuration (or vice versa). The addition of Fe impurity also significantly increases the energy barrier (by 0.039 eV on average) for the surface migration of the clusters.

Nanoindentation methods

Partial loading & unloading indentation experiments were performed using Hysitron TI950. For each experiment, 20 cycles that consist of loading-holding-unloading segments were conducted. For a single cycle, 0.5 s, 1 s and 0.5 s was set for loading, holding and unloading, respectively. Different maximum loads were applied for different specimens to ensure the maximum contact depth is ~ 15% of the total film thickness. At least 10 indentation experiments were carried out for each sample and more than one hundred hardness or modulus data in plateau regions were collected. 20 indents with contact depth of ~ 150 nm were conducted using Fisherscope 2000XYp on each sample to recheck the hardness values.

Stress-strain calculations for deformation volume

FIB polishing normal to the pillar axial direction caused tapering of the pillars, the taper angle of which was measured to be 2.8 ± 0.6˚ on average. To determine the engineering stress-strain curves from the compressions, the cross section at half height was used as the representative area. As such, engineering stress calculated in this study represents a lower bound stress experienced by pillars. The influence of elastic deformation of the Si substrate and the diamond tip on the measurement of strain was estimated by considering the pressed elastic half-space derived by Sneddon. The valid displacement in this study is defined as:

$$u = u_{mea} - \frac{1-v_{dia}^2}{E_{dia}}\left(\frac{F}{d_{it}}\right) - \frac{1-v_{Si}^2}{E_{Si}}\left(\frac{F}{d_b}\right) \quad (1)$$

where u_{mea}, F are the measured displacement and force, respectively. d_{it}, d_b represent the top and bottom diameter of pillars. E_{dia} and ν_{dia} denote the elastic modulus and Poisson ratio of the diamond flat punch, taken to be 1140 GPa and 0.07, respectively. Likewise, The E_{Si} and ν_{Si}

denote the elastic modulus and Poisson ratio of the Si (111) substrates, and are 189 GPa and 0.26, respectively.[6]

The specific deformation structure indicates that the formula of the homogeneous deformation model to convert the true stress, *i.e.* $\sigma_t = \sigma_e(1-\varepsilon_e)$, is not applicable to the upper deformed volume where deformation concentrates. Based on the real-time deformation captured from the *in situ* compression videos, the spontaneous top, middle and bottom diameters of the pillars were measured at varying displacements. It is found that the gain of the top circular plane diameter is approximately linearly proportional to the ongoing displacement. The spontaneous true stress of the deformed volume can be estimated using the formula, $\sigma_t = \frac{F}{A_{mdv}} = \frac{4F}{\pi(d_{mdv})^2}$, where A_{mdv} and d_{mdv} are the real-time area and diameter of the middle of the deformed volume, respectively, and F is the measured force. To obtain the d_{mdv}, the d_t ($d_t = d_{mdv}$) and d_b should be determined first. The dt is defined as $d_t = d_{it} + \alpha u$, were dit is the initial top circular plane diameter and α is the dilation parameter and u is displacement. The relations between d_t and the displacement, u, for Al-2.5, 5.9 at.%Fe pillars are determined to be $d_t = 450 \pm 15 + 0.6 \pm 0.12\,u$ and $d_t = 418 \pm 11 + 0.93 \pm 0.1u$, respectively (**Figure S**5a). Assume the travelling speed of the dilation of the bottom surface of the reverse conical frustum, *i.e.* the deformed volume, along the pillar axial direction is constant at a given strain rate. According to the dilation synchronized to the ongoing displacement, the speed can be approximately estimated from the first observation of the dilation at half height of the pillars. As a result, the varying bottom diameter of the deformed volume, d_{bdv}, originating from the tapering angle, can be defined as $d_{bdv} = d_{it} + \frac{(d_{im} - d_{it})u}{u_c}$, where the initial diameters of the top and the middle of the pillars are given by d_{it} and d_{im}, respectively, and u is the total displacement and the u_c is the critical displacement where the first dilation event is captured at the half height of the pillars. d_{mdv} is

calculated from $d_{mdv} = \frac{d_t + d_{bdv}}{2}$. The spontaneous circular plane area of the middle of the deformed volume, A_{mdv}, is deduced as:

$$A_{mdv} = \pi\left(\frac{2d_{it} + \alpha u + \frac{(d_{im} - d_{it})u}{u_c}}{4}\right)^2 \quad (2)$$

Please note that the onset of plasticity of true stress-strain curves used to predict the plasticity of the deformed volume represent the upper bound of the yield strength as a result of $A_{mdv} = \frac{\pi {d_{it}}^2}{4}$ at zero strain (**Figure S**5c). The possible punch/pillar misalignment and/or compliance with substrate make the precise determination of yield strength challenging and the estimated modulus from the elastic loading slope deviates. Strain hardening exponent, n, were deduced from the regimes on the true stress-strain curves where the contact had been established in a steady flow condition to minimize the initial stiffness error and ensure the stress counted as yield point beyond the first yield event. The Holloman equation, $\sigma = K\varepsilon^n$, with K being the hardening coefficient, is used to deduce the strain hardening exponent, n, at 0.2-0.4 to 5 % offsets.

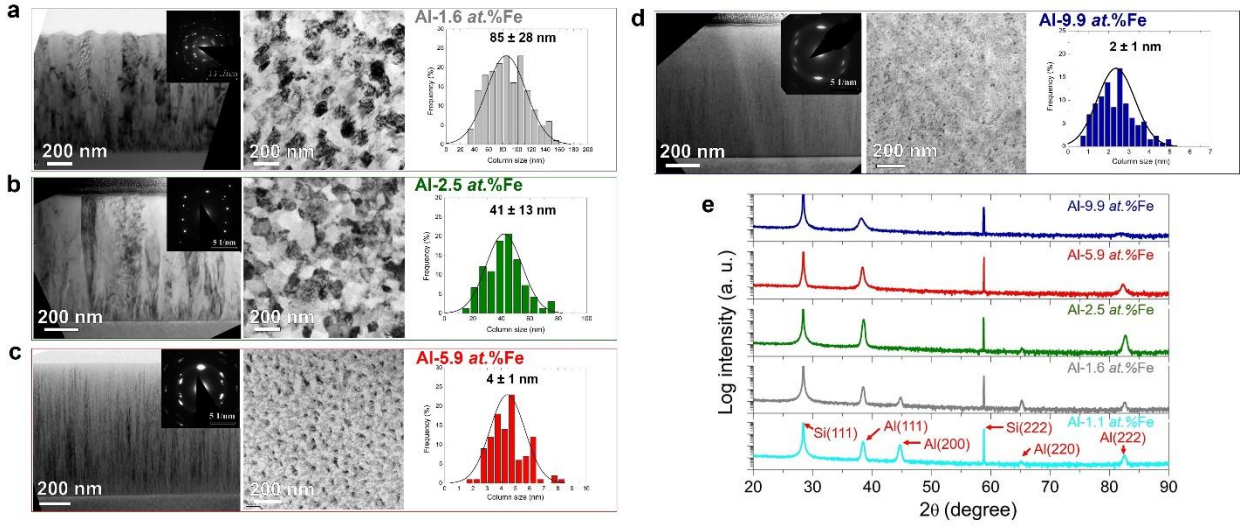

Figure S1. Microstructural and crystallographic information of Al-xFe (x = 1-10 at.%) films: bright-field cross-section and plan-view TEM micrographs and columnar grain size distributions of (a) Al-1.6%Fe; (b) Al-2.5%Fe (c) Al-5.9% Fe and (d) Al- 9.9%Fe. (d) XRD profiles of as-deposited Al-xFe (x = 1-10 at.%) films. The (111) texture is found improved by adding more Fe solutes into Al matrix.

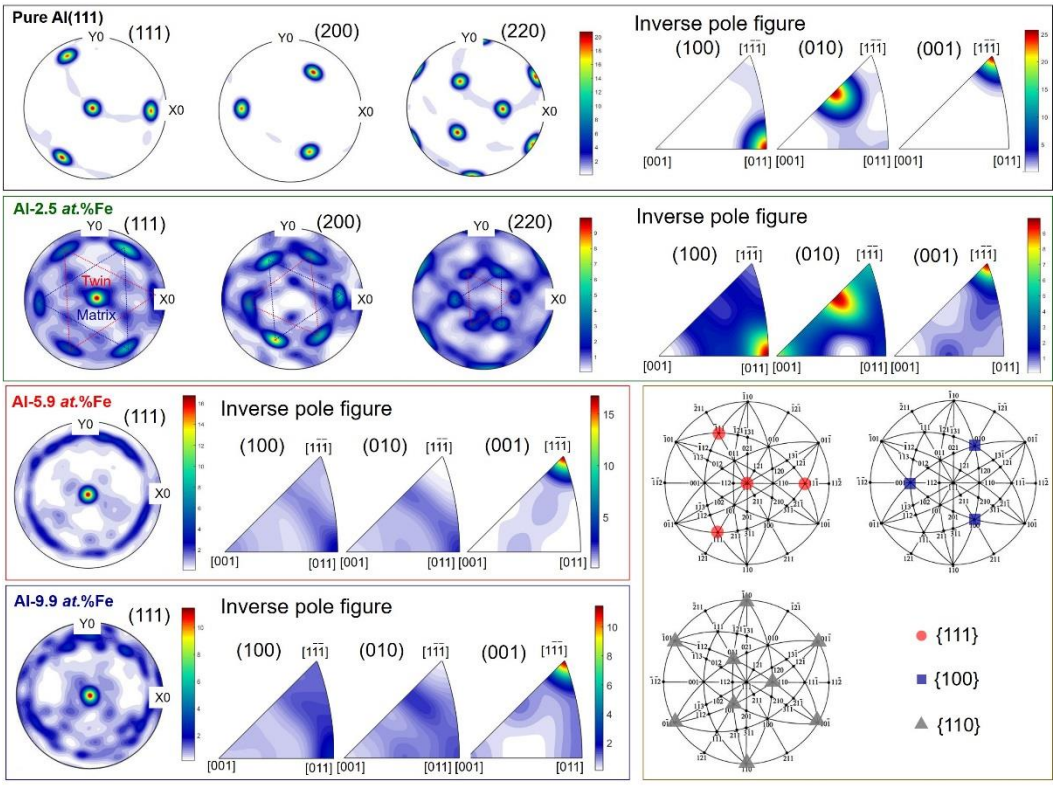

Figure S2. XRD pole figure measurements of the Al-xFe (x = 1-10 at.%) films. (111), (200) and (220) pole figures and corresponding inverse pole figures of monolithic Al(111) and Al-2.5%Fe films. Comparisons of (111) pole figures show that monolithic Al has 3-fold symmetry, whereas a six-fold symmetry of equally bright {111} poles emerge in Al-2.5%Fe, indicative of a large fraction of twin variants in alloyed films. For Al-5.9%Fe and Al-9.9%Fe, the small columnar grains, less than 5 nm, undergo slight in-plane as well as out-of-plane rotations based

on the cross-section TEM analyses. The small local misorientation for nanocolumns leads to an accumulative effect and causes the fiber-like texture in (111) pole figure for Al-5.9%Fe and Al-9.9%Fe specimens, whereas the XTEM analyses unveiled that the nanocolumns remain twin relations despite out-of-plane rotation for several degrees.

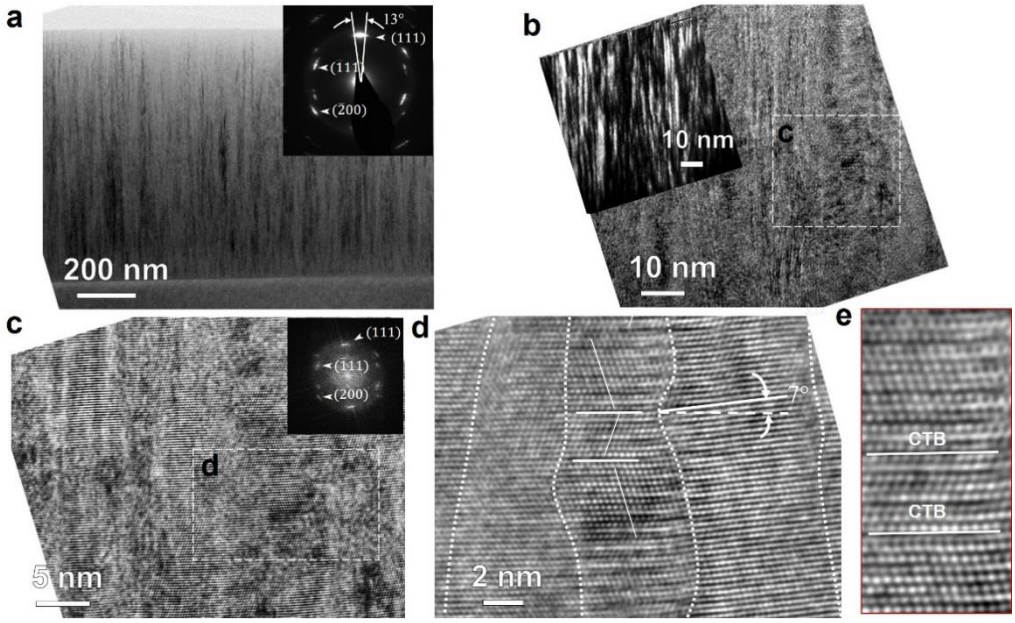

Figure S3. Microstructure of Al-5.9 at.% Fe. (a) The cross-section TEM image of the Al-5.9%Fe specimen. The average grain size is ~ 4 nm. The SAED as inset shows the film is (111) texture and typical twin diffraction pattern. The selected area covered roughly 50 columns, suggestive of a high twin fraction. (b) The magnified micrograph and the inserted corresponding dark-field TEM images show nanoscale columnar grains. (c) HRTEM image corresponding to the selected area from **Figure S**3b also shows the formation of nanocolumns and boundaries. (d) The HRTEM micrograph of several adjacent columns demonstrates the formation of twinned patches of 9R phase in the middle domain. When column size falls below ~10 nm, CTBs

commonly exist, but are decorated with stacking faults. (e) High-density 9R, CTBs and other stacking faults are frequently observed in the domains.

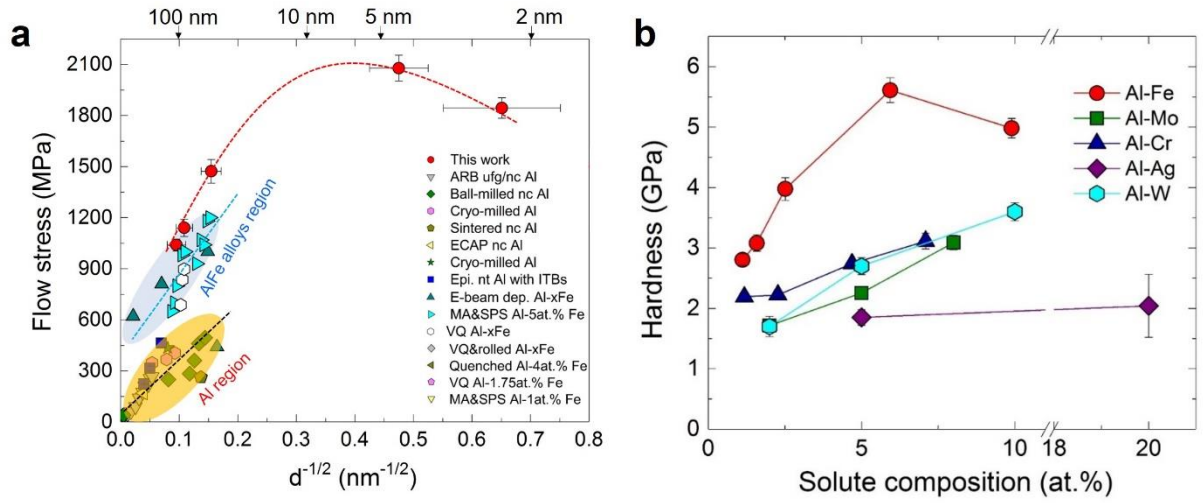

Figure S4. (a) **The Hall-Petch plot for the Al-Fe specimens and the selected ufg and nc monolithic Al and Al-xFe alloys processed *via* different techniques.** In comparison to the monolithic Al and Al-xFe alloys, the sputtered Al-Fe films have exceptionally high flow stress (hardness/2.7). In **Figure S**4a, ultrafine-grained (ufg) and nanocrystalline (nc) monolithic Al [7] and Al-Fe alloys [8] treated by aging or other techniques are cited. Notes: ARB, ECAP, MA, SPS and VQ denote accumulative roll bonding, equal channel angular pressing, mechanical alloying, spark plasma sintering and vapor quenching, respectively. (b) **Hardness *vs.* solute atom concentration of a various sputtered Al alloys with selective solutes.** Effect of various solute atoms on hardness of Al alloys prepared by magnetron sputtering. Hardness *vs.* solute atom concentration of a various sputtered Al alloys with selective solutes. For a variety of solute-incorporated Al alloys, the hardness could hardly exceed ~ 3.5 GPa as solute concentration is equal to or less than 10 at.%, which highlights the vital role of the Fe solutes in the high-strength nt Al-Fe alloys films.

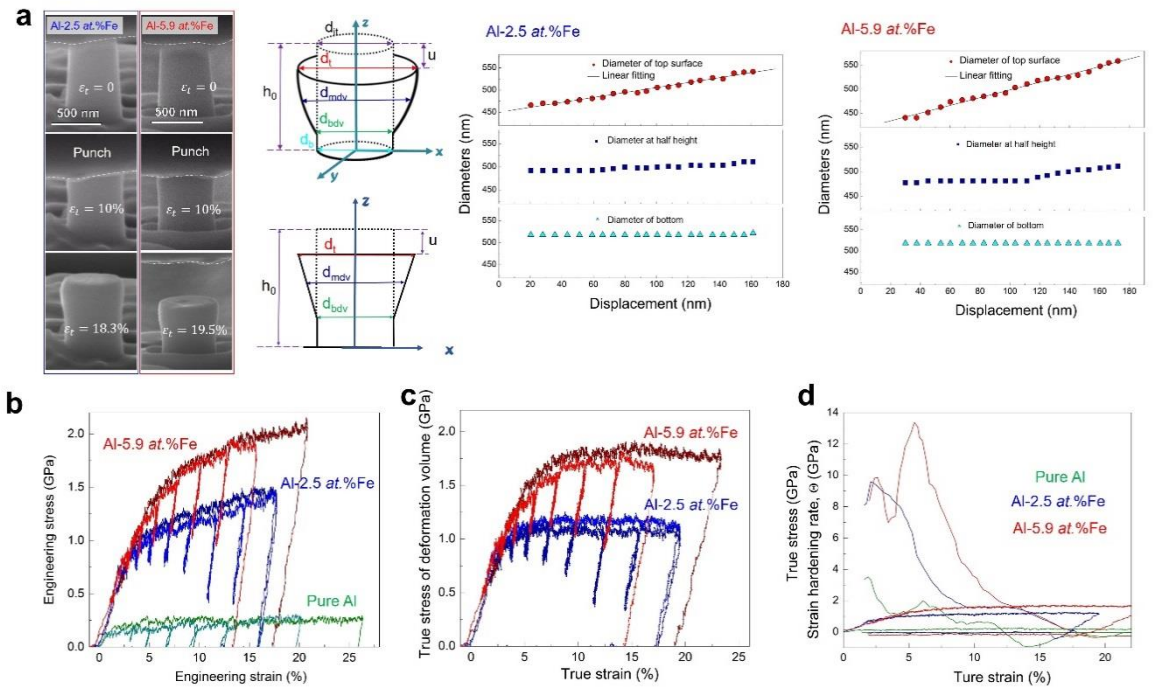

Fig.S5. Methodology to estimate the true stress-strain curves of the deformation volume of nt Al-xFe alloys. (a) Methodology to estimate the true stress-strain curves of the deformation volume of nt Al-xFe alloys. The specific deformation structure indicates that the formula of the homogeneous deformation model to convert the true stress, *i.e.* $\sigma_t = \sigma_e(1-\varepsilon_e)$, is not applicable to the upper deformed volume where deformation concentrates. Based on the real-time deformation captured from the *in situ* compression videos, the spontaneous top, middle and bottom diameters of the pillars were measured at varying displacements. It is found that the gain of the top circular plane diameter is approximately linearly proportional to the ongoing displacement. The spontaneous true stress of the deformed volume can be estimated using the formula, $\sigma_t = \frac{F}{A_{mdv}} = \frac{4F}{\pi(d_{mdv})^2}$, where A_{mdv} and d_{mdv} are the real-time area and diameter of the middle of the deformed volume, respectively, and F is the measured force. To obtain the d_{mdv}, the d_t ($d_t = d_{mdv}$) and d_b should be determined first. The dt is defined as $d_t = d_{it} + \alpha u$, were dit

is the initial top circular plane diameter and α is the dilation parameter and u is displacement. The relations between d_t and the displacement, u, for Al-2.5, 5.9 at.%Fe pillars are determined to be $d_t = 450 \pm 15 + 0.6 \pm 0.12\,u$ and $d_t = 418 \pm 11 + 0.93 \pm 0.1u$, respectively. (b) Representative engineering stress-strain curves. Two types of experiments were performed for each specimen, including regular uniaxial loading, and a series of partial loading-unloading studies. The partial loading-unloading experiments permit the determination of elastic modulus of specimens. The two sets of experiments yield similar stress-strain curves. (c) The true stress-strain curves of the deformation volume of Al-2.5%Fe and Al-5.9%Fe specimens. On the contrary to the conventional softening, the flow stress for the nt Al-xFe alloys can be sustained. (d) Strain hardening rate, $\Theta = {d\sigma}/{d\varepsilon}$, of pure Al, Al-2.5%Fe and Al-5.9%Fe.

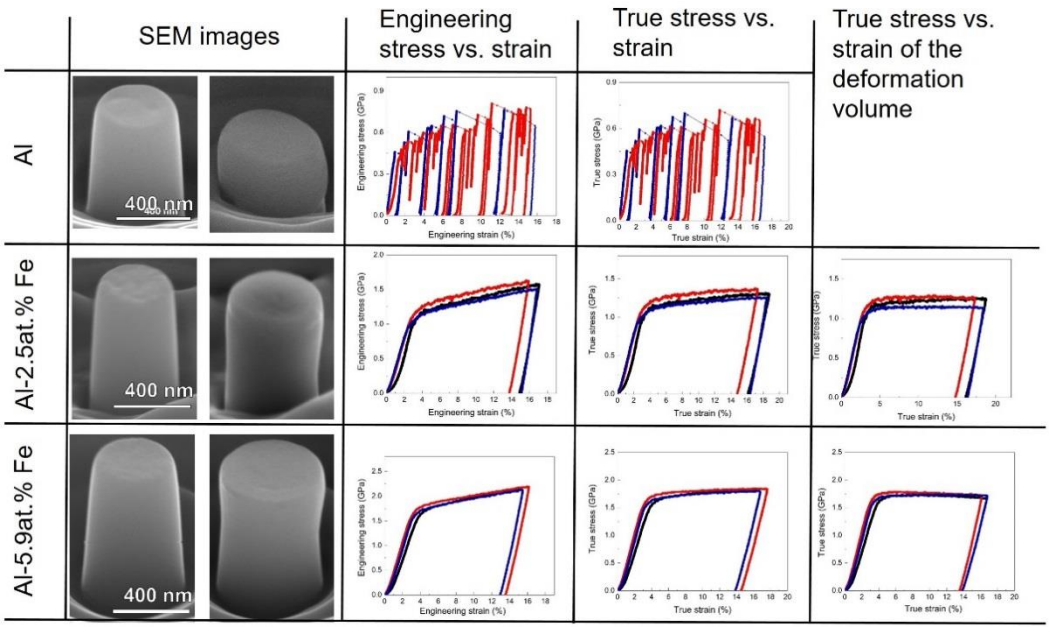

Figure S6. *Ex situ* pillar compression results of monolithic Al and Al-xFe (x = 2.5 and 5.9 at.%) specimens. SEM micrographs of pillars before and after compressions. A remarkable dislocation burst phenomenon were captured on the stress-strain curves of the pure Al. The

methodology developed in comprehending the *in situ* compression results was applied to the *ex situ* compression results. The top diameter of the grain is considered linearly proportional to the increase in strain and the deformation volume spreading speed in the pillar axial direction at a given strain rate at certain Al-Fe composition is assumed to be constant.

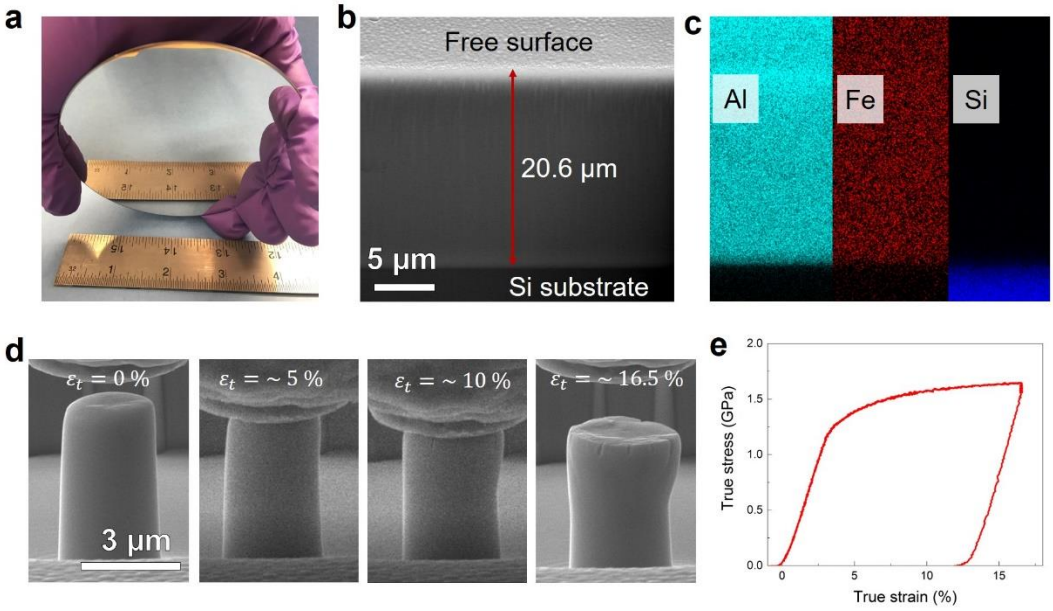

Figure S7. Fabrication of a 20 μm thick Al-6 at.% Fe coating on Si wafer and *in situ* compressions on 3 μm diameter micropillars of Al-6 at.% Fe specimens. (**a**) Digital micrograph of ~ 20 μm thick Al-6 at.% Fe coating that well adheres to Si wafer with 3 inch in diameter. (**b**) Cross-section SEM micrograph of the 20 μm thick Al-6 at.% Fe coating and (**c**) corresponding EDS patterns of Al, Fe and Si. (d) *In situ* compression tests were applied on micropillars of Al-6 at.% Fe. The stress *vs.* strain curves are in good agreement with results obtains from micropillars with 500 nm diameter presented in main text. These micropillars of large diameters show exceptionally high flow stress (> 1.5 GPa) and strain hardening ability.

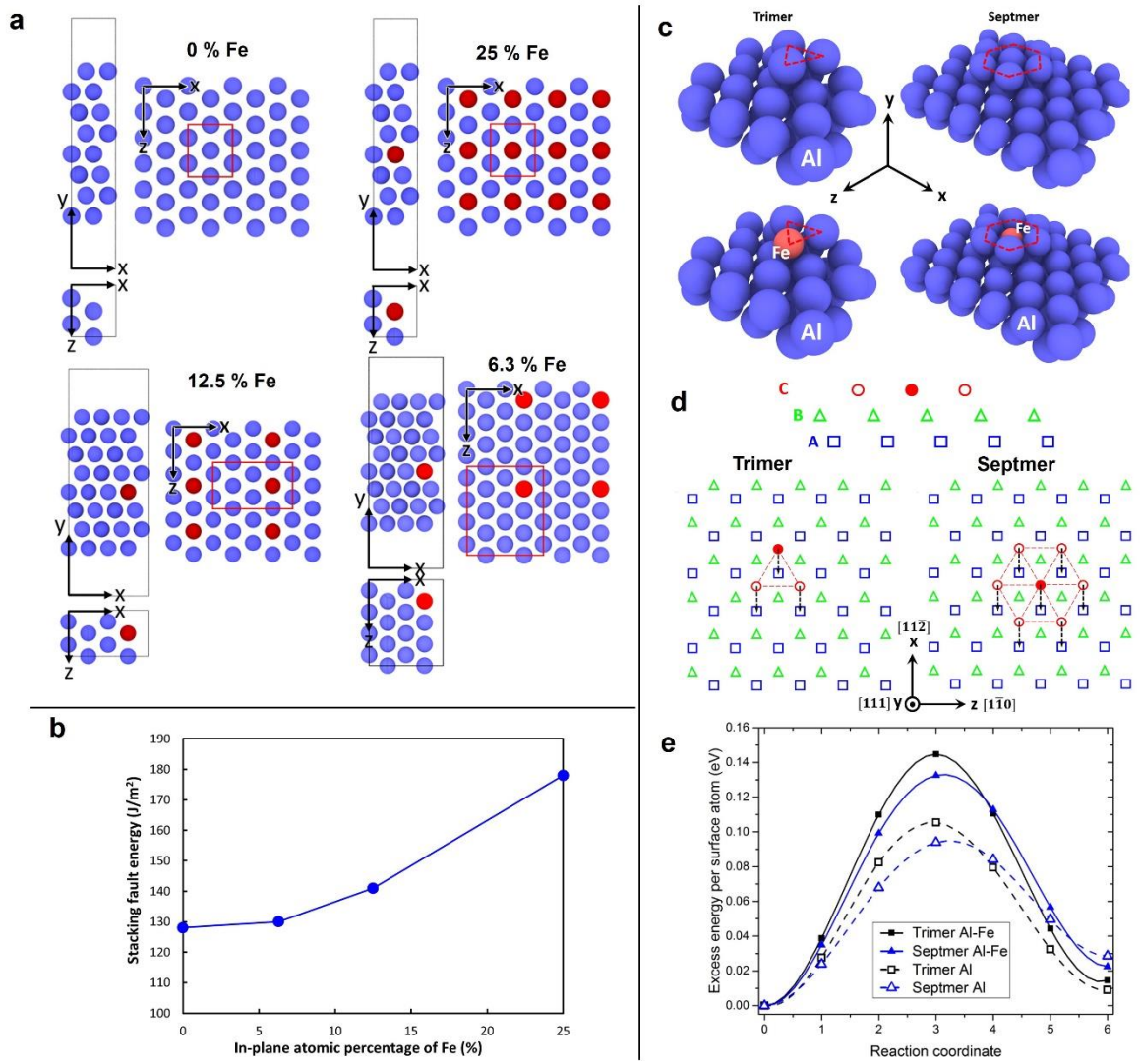

Figure S8. (a) **Atomistic structures for calculations of bulk stacking fault energies.** In each sub-figure, an expanded view is provided to show the atomic percentage of the Fe impurity (in-plane atomic percentage: 0, 6.3, 12.5 and 25 %) on the slip plane. The red box shows the periodic computational cell size in the expanded view. (b) **Stacking fault energy of Al as a function of in-plane atomic percentage of Fe.** (c) **Atomistic configurations to calculate the stacking fault energies of surface atomic clusters.** (d) **Schematic representation of the paths of the surface trimer and septmer for the calculation of their stacking fault energies**. (e)

Excess energy per surface atom *vs.* reaction coordinate curves for various types of surface atomic clusters for Al-3.1at% Fe.

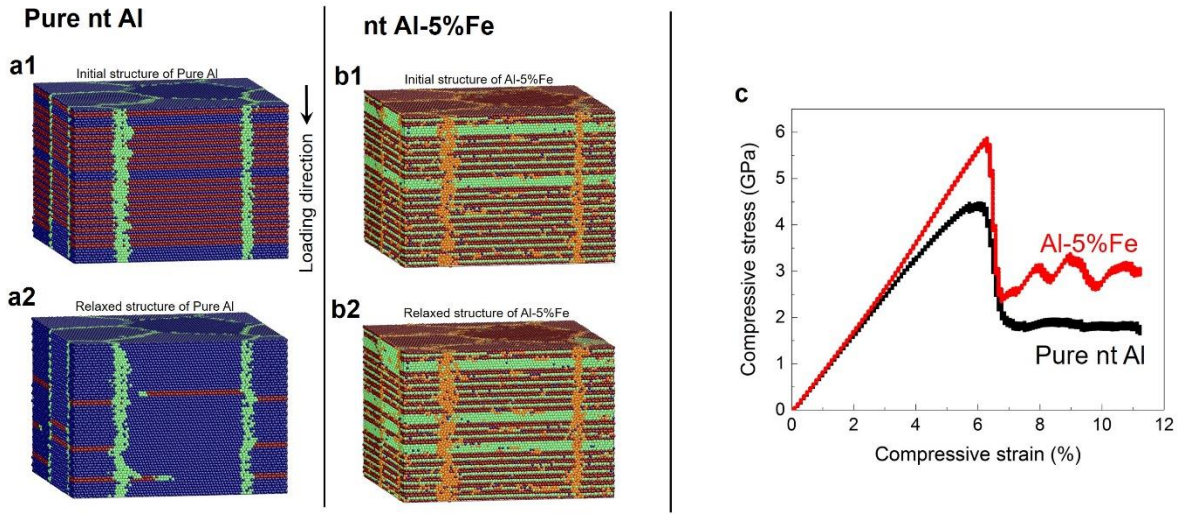

Figure S9. MD simulations: 9R stability in monolithic nt Al and Al-5%Fe at room temperature. (a, b) In the MD simulations, the 9R column is set as 10 nm in width. Model dimensions are designed as x= 20 nm, z=20 nm, y = 14 nm, and boundaries in three directions are periodically repeated. Both cases have the same initial structure. The difference is 5% Al atoms are substituted by Fe atoms (atoms are colored according to Common-Neighbor Analysis: in pure Al, red-stacking fault; blue-Al matrix atoms; green-grain boundaries and defects; in Al-5%Fe, red-stacking fault; blue-Fe solutes; brown-GBs and defects; green-Al matrix atoms-centered cubic structure). After 50 ps, 9R structures recover in Al (see Movie S4). In contrast 9R structures in Al-Fe are mostly stable except recovery at few places (see Movie S5). (c) **Calculated compressive stress *vs.* strain curves of pure Al and Al-5%Fe. Al-5%Fe exhibits high stress and large strain hardening.**

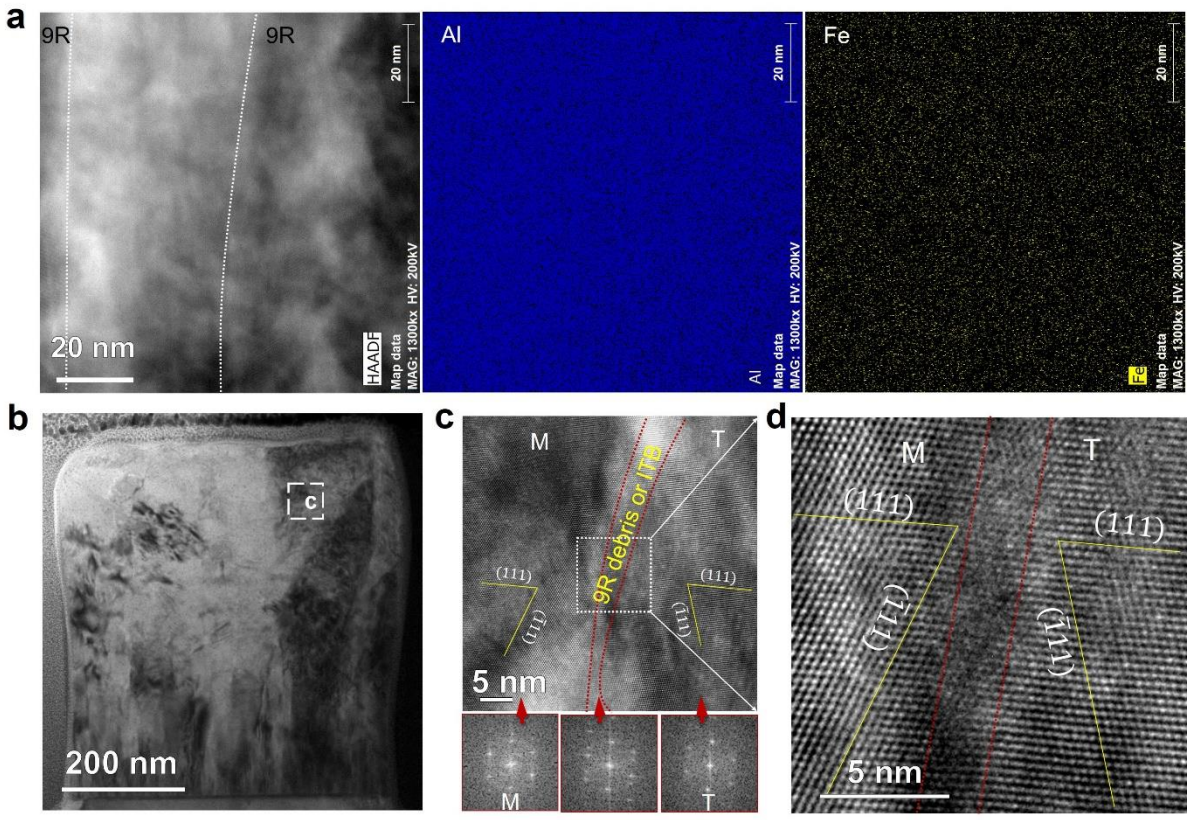

Figure S10. (a) **Super X EDS and STEM of the Al-2.5%Fe (cross-sectional STEM).** The EDS mapping shows homogeneous distribution of Fe solutes. (b-d) **Post-mortem TEM micrographs of deformed Al-2.5 at.% Fe.** (b) Post-mortem bright-field TEM image of deformed Al-2.5 at.% Fe. (c, d) TEM micrograph taken in a region near the pillar top of Al-2.5%%Fe after compressive strain of ~ 20%, where deformation was initiated. 9R phase shrinks to debris of ITBs based on the post-mortem TEM analysis. Narrow boundary is bounded by two twinned columns in lieu of broad 9R phase. The narrow boundary is considered 9R debris or ITB. The 9R mobility (during deformation) might cause the grain coarsening in regions near the pillar top.

Table S1. Summary of columnar grain size, hardness and modulus of the pure Al and Al-Fe alloys. Compositions are all in atomic percentage.

Specimen	Columnar size (nm) TEM	Hardness (GPa), TI950	Indentation modulus (GPa), TI950	Hardness (GPa), Fischerscope 2000XYp
Pure Al	400 ± 93	0.8 ± 0.03	-	0.8 ± 0.07
Al-1.1%Fe	110 ± 34	2.5 ± 0.14	107 ± 9	2.8 ± 0.10
Al-1.6%Fe	85 ± 28	2.8 ± 0.18	107 ± 10	3.1 ± 0.14
Al-2.5%Fe	41 ± 13	3.5 ± 0.08	115 ± 11	4.0 ± 0.19
Al-5.9%Fe	4 ± 1	5.5 ± 0.08	115 ± 8	5.6 ± 0.20
Al-9.9%Fe	2 ± 1	4.7 ± 0.18	115 ± 11	5.0 ± 0.16

Table S2. Details of atomistic models shown in **Figure S**8**.**

Model	Figure	Model size (No. of atoms)	Atomic percentage (in-plane)	Atomic percentage (overall)
1	8a	32	0%	0%
2	8b	32	25%	3.10%
3	8c	64	12.50%	1.60%
4	8d	128	6.30%	0.80%

References

[1] P. Giannozzi, S. Baroni, N. Bonini, M. Calandra, R. Car, C. Cavazzoni, D. Ceresoli, G. L. Chiarotti, M. Cococcioni, I. Dabo, A. Dal Corso, S. de Gironcoli, S. Fabris, G. Fratesi, R. Gebauer, U. Gerstmann, C. Gougoussis, A. Kokalj, M. Lazzeri, L. Martin-Samos, N. Marzari, F. Mauri, R. Mazzarello, S. Paolini, A. Pasquarello, L. Paulatto, C. Sbraccia, S. Scandolo, G. Sclauzero, A. P. Seitsonen, A. Smogunov, P. Umari, R. M. Wentzcovitch, *J. Phys-Condens Mat.* **2009**, *21*.

[2] J. P. Perdew, K. Burke, M. Ernzerhof, *Phys. Rev. Lett.* **1996**, *77*, 3865.

[3] K. Lejaeghere, G. Bihlmayer, T. Bjorkman, P. Blaha, S. Blugel, V. Blum, D. Caliste, I. E. Castelli, S. J. Clark, A. Dal Corso, S. de Gironcoli, T. Deutsch, J. K. Dewhurst, I. Di Marco, C. Draxl, M. Dulak, O. Eriksson, J. A. Flores-Livas, K. F. Garrity, L. Genovese, P. Giannozzi, M.

Giantomassi, S. Goedecker, X. Gonze, O. Granas, E. K. U. Gross, A. Gulans, F. Gygi, D. R. Hamann, P. J. Hasnip, N. A. W. Holzwarth, D. Iusan, D. B. Jochym, F. Jollet, D. Jones, G. Kresse, K. Koepernik, E. Kucukbenli, Y. O. Kvashnin, I. L. M. Locht, S. Lubeck, M. Marsman, N. Marzari, U. Nitzsche, L. Nordstrom, T. Ozaki, L. Paulatto, C. J. Pickard, W. Poelmans, M. I. J. Probert, K. Refson, M. Richter, G. M. Rignanese, S. Saha, M. Scheffler, M. Schlipf, K. Schwarz, S. Sharma, F. Tavazza, P. Thunstrom, A. Tkatchenko, M. Torrent, D. Vanderbilt, M. J. van Setten, V. Van Speybroeck, J. M. Wills, J. R. Yates, G. X. Zhang, S. Cottenier, *Science* **2016**, *351*.

[4] X. Y. Liu, F. Ercolessi, J. B. Adams, Model Simul Mater Sc 2004, 12, 665; G. Lu, N. Kioussis, V. V. Bulatov, E. Kaxiras, *Phys Rev B* **2000**, *62*, 3099.

[5] P. Haas, F. Tran, P. Blaha, *Phys Rev B*, **2009**, *79*; P.H.T. Philipsen, E.J. Baerends, *Phys Rev B*, **1996**, *54*, 5326; W.P. Davey, *Phys Rev*, **1925**, *25*, 753.

[6] I.N. Sneddon, *International Journal of Engineering Science*, **1965**, *3*, 47; C.P. Frick, B.G. Clark, S. Orso, A.S. Schneider, E. Arzt, *Mat Sci Eng a-Struct*,**2008**, *489*, 319.

[7] X.K. Sun, H.T. Cong, M. Sun, M.C. Yang, *Metall Mater Trans A*, **2000**, *31*, 1017; R.W. Hayes, D. Witkin, F. Zhou, E.J. Lavernia, *Acta Mater*, **200**4, *52*, 4259; H.J. Choi, S.W. Lee, J.S. Park, D.H. Bae, *Mater Trans*, **2009**, *50*, 640; K. Maung, J.C. Earthman, F.A. Mohamed, *Acta Mater*, **2012**, *60*, 5850; Y. Saito, N. Tsuji, H. Utsunomiya, T. Sakai, R.G. Hong, Scripta Mater, **1998**, 39, 1221; G.J. Raab, R.Z. Valiev, T.C. Lowe, Y.T. Zhu, *Materials Science and Engineering: A*, **2004**, *382*, 30.

[8] H. Sasaki, K. Kita, J. Nagahora, A. Inoue, *Mater Trans*, **2001**, *42*, 1561; T.T. Sasaki, T. Ohkubo, K. Hono, *Acta Mater*, **2009**, *57*, 3529; T. Mukai, S. Suresh, K. Kita, H. Sasaki, N. Kobayashi, K. Higashi, A. Inoue, *Acta Mater*, **2003**, *51*, 4197; M.H. Jacobs, A.G. Doggett, M.J. Stowell, *J Mater Sci*, **1974**, *9*, 1631; C.L. Mendis, H.P. Jhawar, T.T. Sasaki, K. Oh-ishi, K. Sivaprasad, E. Fleury, K. Hono, *Mat Sci Eng a-Struct*, **2012**, *541*, 152; P.G. Partridge, *J Mater Sci*, **1986,** *21*, 3211.